Highlighting work from the Varanasi Research Group, MIT, Cambridge USA.

Title: How droplets nucleate and grow on liquids and liquid impregnated surfaces

While nucleation is most likely to occur at the liquid−air interface, the liquid viscosity plays a key role in determining the overall growth of droplets.

ROYAL SOCIETY OF CHEMISTRY

www.softmatter.org

PAPER

CrossMark
←click for updates

How droplets nucleate and grow on liquids and liquid impregnated surfaces†

Sushant Anand,*[a] Konrad Rykaczewski,[b] Srinivas Bengaluru Subramanyam,[c] Daniel Beysens[de] and Kripa K. Varanasi[a]

Condensation on liquids has been studied extensively in context of breath figure templating, materials synthesis and enhancing heat transfer using liquid impregnated surfaces. However, the mechanics of nucleation and growth on liquids remains unclear, especially on liquids that spread on the condensate. By examining the energy barriers of nucleation, we provide a framework to choose liquids that can lead to enhanced nucleation. We show that due to limits of vapor sorption within a liquid, nucleation is most favoured at the liquid–air interface and demonstrate that on spreading liquids, droplet submergence within the liquid occurs thereafter. We provide a direct visualization of the thin liquid profile that cloaks the condensed droplet on a liquid impregnated surface and elucidate the vapour transport mechanism in the liquid films. Finally, we show that although the viscosity of the liquid does not affect droplet nucleation, it plays a crucial role in droplet growth.

1. Introduction

Condensation of vapor on a surface can occur either in filmwise or dropwise mode. For many applications including power generation, water harvesting, desalination, and thermal management, dropwise condensation is preferred as it expedites the removal of the condensate from the surface resulting in a significant increase in condensation heat transfer.[1–6] The magnitude of this increase is related to the three stages of a droplet "life" on a surface: nucleation, growth, and departure. Various routes of optimizing these aspects of dropwise condensation *via* surface engineering have been proposed. Functionalizing the surface to obtain a hydrophobic surface chemistry and combining it with nano/micro-texturing to achieve superhydrophobicity are some of the ways explored to reduce droplet adhesion as measured through contact angle hysteresis.[5,7–9] In some cases, the reduced adhesion on superhydrophobic surfaces can also lead to micro-droplet ejection upon coalescence with neighbouring droplets.[10–12] However,

under high subcooling conditions, nucleation of a large density of nanoscale droplets within the texture of superhydrophobic surfaces leads to the formation of a liquid film on the surface.[13–15] In order to overcome such challenges, an alternative surface design with composite solid–liquid materials has gained significant attention recently.[16–22] Such composite materials consist of nano/micro textured low surface energy surfaces impregnated with a liquid (henceforth also referred to as oil, and denoted with subscript 'o') immiscible with the fluid (henceforth denoted with subscript 'w') to be repelled. These liquid-impregnated surfaces (LIS) shed a wide variety of fluids[17] with minimal contact angle hysteresis[16–24] and have been recently shown to significantly increase dropwise condensation heat transfer of fluids with widely ranging surface tensions.[21]

The three stages of condensation (nucleation, growth, and departure) on LIS are greatly influenced by the properties of the impregnating liquid. It has been reported that the nucleation energy barrier for condensation is lowered[19] and nucleation rates are enhanced[25] on LIS, when compared to superhydrophobic surfaces with identical solid surface chemistry. However, the role of oil properties on nucleation remains unclear. Furthermore, an oil may "cloak" the condensing droplets if the spreading coefficient of the oil with respect to the droplet is positive, *i.e.* $S_{ow(a)} = \gamma_{wa} - \gamma_{oa} - \gamma_{wo} > 0$ (γ_{wa}, γ_{oa} and γ_{wo} refer to the surface tension of the droplet, surface tension of the oil, and the interfacial tension between the oil-droplet, respectively), and this leads to a suppression of droplet growth.[19] However, even in the presence of the cloaking mechanism, sustained growth of water droplets on a polymer,[25] a pure solvent[26] or solvent–polymer mixtures with solvent spreading coefficient $S_{ow(a)} > 0$ has been observed.[27–30] These

[a]*Department of Mechanical Engineering, Massachusetts Institute of Technology, Cambridge, MA, USA. E-mail: sushant@mit.edu; Tel: +1-617-253-5066*

[b]*School for Engineering of Matter, Transport and Energy, Arizona State University, Tempe, AZ, USA*

[c]*Department of Materials Engineering, Massachusetts Institute of Technology, Cambridge, MA, USA*

[d]*PMMH/ESPCI & CNRS UMR 7636, Universités Paris 6 & Paris 7, 10 rue Vauquelin, 75005 Paris, France*

[e]*Service des Basses Températures, CEA-Grenoble & Université Joseph Fourier, Grenoble, France*

contrasting observations highlight the need to understand the mechanism underlying droplet nucleation and growth on oils.

In this study, we use theoretical and experimental approaches to understand nucleation and growth of droplets on immiscible oils. Here, we have identified the different pathways for nucleation on LIS and clarified the nucleation energetic barriers associated with them using classical nucleation theory. Our results indicate that the nucleation energy barrier is significantly lowered within the oil as compared to nucleation in air for some oil–solid combinations – provided that the critical supersaturation is available. However, in a subcooled oil, the vapor–sorption process prevents the vapor to achieve supersaturation in the oil, so that the oil–air interface is the most favored site for nucleation. We investigate the mechanisms accompanying growth of droplets on cloaking oils, and used the cryogenic Focused Ion Beam-Scanning Electron Microscopy (cryo-FIB-SEM) to uncover phenomena such as the presence of submerged droplets within the oil, and the oil nanofilm profile around a condensed droplet on LIS. Finally, we have carried systematic investigation of the effect of oil viscosity on droplet coalescence and growth. Our results could provide important insights into the dynamics of condensation on liquids for applications such as breath figure templating,[27–31] materials synthesis,[32] and oil recovery by steam injection.[33,34]

2. Materials and methods

2.1 Preparation of silicon samples

Arrays of square microposts of 10 μm height (h), 10 μm width (a) and 10 μm edge-to-edge spacing (b) were patterned via photolithography and etched via deep reactive ion etching (DRIE) on two centimetre square silicon substrates (p-type ⟨100⟩, 650 μm thick). Thereafter the samples were cleaned using piranha solution and subsequently coated with OTS (octadecyltrichlorosilane, Sigma Aldrich) using a solution deposition method. Silanization of the sample renders the surface hydrophobic and allows the oil to stably adhere to the surface in the presence of water.

2.2 Liquids used in the current study

The liquids used in the current study were silicone oils with a viscosity of 10 cSt ($\rho_o = 935$ kg m^{-3}, $M_o \sim 1250$), 100 cSt ($\rho_o = 960$ kg m^{-3}, $M_o = 5970$) and 1000 cSt ($\rho_o = 970$ kg m^{-3}, $M_o = 28\,000$) purchased from Sigma-Aldrich. Other liquids used in the study (tetradecane, hexadecane, 1-bromonaphthalene, 1-butyl-3-methylimidazolium bis(trifluoromethylsulfonyl)imide ([BMIm$^+$][Tf2N$^-$])) were also purchased from Sigma Aldrich.

2.3 Preparation of impregnated samples

The silanized samples were dipped in a reservoir of the impregnating oil with a dip-coater (KSV Nima Multi Vessel Dip Coater). In order to prevent excess oil on the samples, they were withdrawn at a controlled velocity V such that the capillary number $\mathrm{Ca} = \mu_o V / \gamma_{oa}$ was less than 10^{-4}.[35]

2.4 Contact angle measurements

Contact angles of the oils on smooth OTS-coated silicon surfaces were measured in the presence of air, as well as water using a Ramé-Hart Model 500 Advanced Goniometer. The interfacial tension between the oils and water was measured using the pendant drop technique on the same device.

2.5 Apparatus for vapor absorption and condensation

An annular steel ring (diameter: 25.4 mm, height: 5 mm) was attached to a smooth silicon surface using an adhesive to hold the oil. The silicon surface was cleaned thoroughly with acetone and isopropanol before attaching to the ring and displayed partially wetting behaviour. After filling the holder with 0.5 ml of 10 cSt silicone oil, the setup was put on a peltier cooler. The peltier temperature was lowered below the room temperature (25 ± 1 °C) to 16 ± 1 °C, but kept above the dew point (13 ± 1 °C) to prevent supersaturation in the air near the setup. After two hours, the temperature of the peltier was lowered to 9 ± 1 °C. Condensation followed within seconds on the surface. Condensation on the oil was observed using a Zeiss AxioZoom microscope fitted with a 'Plan APO-Z 1.5× lens' and a polarizer at 260× magnification. The videos were recorded using a Nikon D-800 camera at a resolution of 1920 × 1080 and 30 fps. The schematic of the experimental setup is shown in the ESI (Fig. S1(a)†).

To determine if nucleation occurred within vapour-saturated oil that was subcooled, 10 cSt silicone oil was used as the test liquid. Deionized water in a flask was bubbled with the dry nitrogen gas to obtain vapour-saturated air. The vapor-saturated air was then bubbled through 15 ml of 10 cSt silicone oil kept in a beaker for three hours. The schematic of this setup is shown in ESI Fig. S1(b).† Thereafter, 10 ml of vapour-saturated silicone oil was extracted in an airtight glass vial of 10 ml capacity with a partially wetting surface. After insulating the glass vial sidewalls, it was cooled to a temperature of −2 °C for a period of three hours. It was made sure that no air bubble remained in the glass vial before it was subjected to cooling. The room temperature was measured as 20 °C and a room humidity of 60% implying a dew point of 12 °C. After three hours, 20 μl of solution was extracted from the glass vial and analysed using the dynamic light scattering (DLS) setup. DLS measurements were performed using DynaPro NanoStar™, capable of identifying droplets in the size range of 0.2–2500 nm hydrodynamic radius. DLS measurements were performed ten times for one extraction volume. The experiment was repeated using three separate samples extracted from the solution.

2.6 Experiment procedure for cryo-FIB-SEM

The Cryo-SEM technique was used to characterize the morphology of various samples. For cross-sectional imaging of oil substrates, we used a modification of the cryogenic Focused Ion Beam-Scanning Electron Microscopy (cryo-FIB-SEM) method, which has recently been used to image water drops,[36] frost and ice growth[37] and adhesion mechanisms on superhydrophobic and liquid impregnated surfaces.[38] Two types of

experiments were performed and analyzed using this technique. In the first experiment water was condensed on silicone oil. Customized copper stubs with holes (2 mm in width and depth) were fabricated to contain the oil. A copper stub was mounted to the cryo-shuttle transfer device and filled with the oil of known viscosity (10, 100 and 1000 cSt). To trigger condensation on silicone oil, the temperature of the entire assembly was decreased using a water ice bath cooled peltier element. The temperature of the stub was monitored using a thermocouple mounted in a hole mounted on the side on the cup. A decrease in oil volume within the stub hole was observed during condensation due to oil displacement by droplets, and spreading of oil on condensed droplets on the copper stub. Then, the stub was plunge-frozen in liquid nitrogen slush at $-210°C$. The sample vacuum transfer, thin metal film grounding, FIB-cutting, and SEM-imaging procedures are described elsewhere.[36,37] The SEM images of the FIB-cross sections were taken at a 52-degree sample stage tilt.

In the second experiment, water droplets were condensed on LIS. Silicon substrates with micropost arrays as described in Section 2.1 were impregnated with silicone oils of 10, 100 and 1000 cSt of viscosity by the method as described in Section 2.3. Thereafter, condensation and the cryo-FIB-SEM analysis were performed with the same methodology as described before for the first experiment.

The identification of the individual phases of oil/water/platinum was obtained by virtue of the imaging contrast combined with *in situ* elemental analysis. In backscattered electron imaging, the contrast of individual phases correlates strongly with their density. Although the densities of water and silicone oils are of similar order, sufficient contrast was observed between these two liquid phases. To ensure proper interpretation of the two phases imaged in FIB milled cross-sections, elemental analysis was also performed using Energy-Dispersive X-ray Spectroscopy (EDS). As in our previous work, spectra corresponding to water consisted primarily of oxygen signals, while those corresponding to silicone oil also contained silicon and carbon peaks. To avoid electron beam heating damage to the cut surface, only point spectra outside of the area of interest were taken. Since the topic of elemental tagging of water and oil was covered in our previous work,[36] the spectra were not saved for presentation.

2.7 Apparatus for condensation observation on LIS

Silicon samples with micropost arrays (described in Section 2.1) were impregnated with silicone oils (with a methodology described in Section 2.3). The samples were kept on a cooling block maintained at a constant temperature of 3 ± 1 °C. All the experiments were performed in an open environment under the same conditions (Room Temperature 20 ± 1 °C and dew point 12 ± 1 °C). The humidity near the sample was continuously monitored using a Sensirion KT-71 humidity sensor. Condensation on the surface was observed using a Zeiss AxioZoom microscope fitted with a 'Plan APO-Z $1.5\times$ lens' and a polarizer at $260\times$ magnification. A Nikon D-800 camera was used to record videos at 1920×1080 and 30 fps. Videos were analyzed

to evaluate droplet growth using ImageJ software.[39] The schematic of the experimental setup is shown in the ESI section (Fig. S1(a)†).

2.8 Image analysis

From the videos, the frames were extracted for analysis of droplet mobility that was performed using ImageJ.[39] Droplet areas were measured for all the droplets in a given frame and from these measurements, the area fraction ($A_{fraction}$) under condensation at a time t occupied by droplets was calculated by

$$\left(A_{fraction}\right)_t = \left(\sum_{i=1}^{N} (\text{Droplet Area})_i\right)_t \bigg/ \text{Frame Area}.$$

The polydispersity or the size variation in droplet sizes in a frame at a time t was calculated as $(\text{polydispersity})_t = D_{w,t}/D_{n,t}$ where $D_{w,t}$ is the weight averaged diameter and given by

$$D_{w,t} = \left(\sum_{i=1}^{N} (\text{Droplet Diameter})_i^2\right)_t \bigg/ \left(\sum_{i=1}^{N} (\text{Droplet Diameter})_i\right)_t$$

and $D_{n,t}$ is the number-averaged diameter given by

$$D_{n,t} = \left(\sum_{i=1}^{N} (\text{Droplet Diameter})_i\right)_t \bigg/ \left(\sum_{i=1}^{N} i\right)_t.$$

3. Results and discussion

3.1 Nucleation states and energetic barriers

On LIS, the impregnating oil can exist in one of the two states – with emergent post tops and fully submerged features.[20] Depending on the state in which oil exists in LIS, nucleation can occur at the solid–air interface (Fig. 1a-State I), within the oil (homogeneous nucleation, Fig. 1a-State II), at the solid–oil interface (heterogeneous nucleation within oil, Fig. 1a-State III), or at the oil–air interface (heterogeneous nucleation on oil, Fig. 1a-State IV). In a recent work, it has been suggested that enhancement in nucleation rate occurs on LIS compared to superhydrophobic surfaces because the presence of 'high surface energy sites' on the submerged solid surfaces results in significantly lower energy barrier in State III compared to State I.[25] However, these observations could also be attributed to the nucleation at the oil–air interface (State IV), as it may also be energetically favourable compared to State I. Nucleation of water droplets on bulk oil surfaces is well known,[26,40] and very large nucleation rates have also been observed on bulk oils.[41,42] Although nucleation at solid–air[4] and oil–air[43,44] interfaces has been examined before, a comprehensive comparison of vapour nucleation in different possible states has been lacking. Such comparison can not only lead to understanding of the energy barriers for nucleation on oils compared to the solid surfaces, but could also be used to choose oils that can enhance or suppress nucleation rates on LIS. Here we examine the free energy barrier of nucleation for these different states in order to identify the most preferable nucleation pathway.

From Classical Nucleation Theory (CNT), the work of cluster formation (W) through nucleation is given as $W(n) = -nkT \ln(\text{SR}) + E$ where n corresponds to the number of molecules in the cluster, SR is the supersaturation, k is the
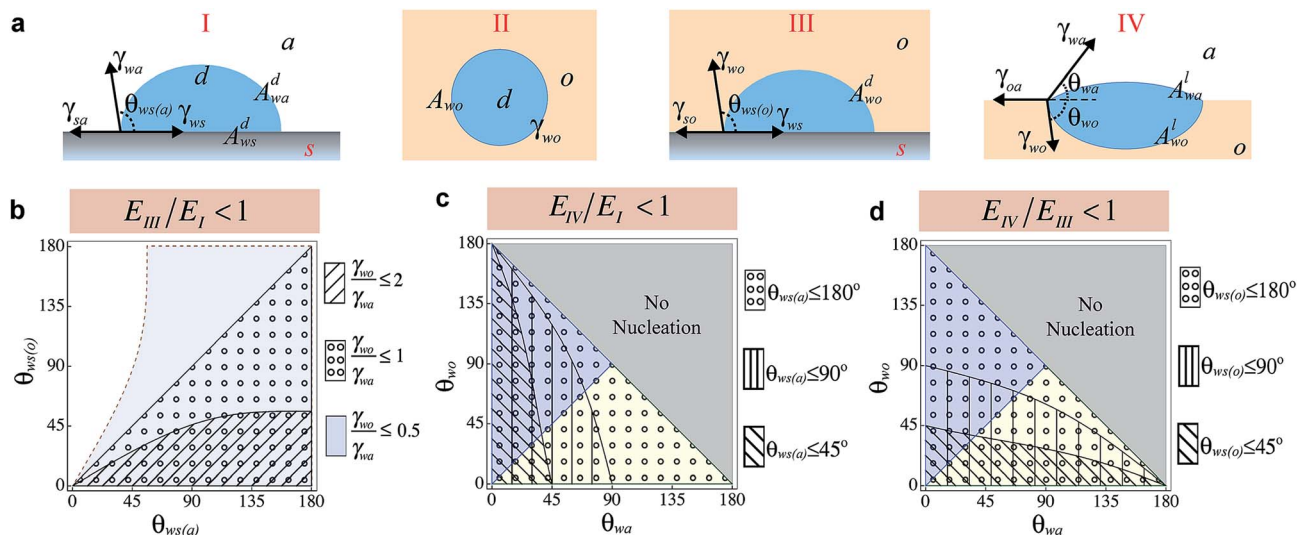
Fig. 1   Nucleation states and regime maps of nucleation preference. (a) Possible pathways of nucleation between a condensing drop and its environment. The subscripts w, a, o and s denote droplet, air, oil and solid interfaces, respectively. The superscripts d and l denote the droplet and lens. In State I and III, A_{ws}^d and A_{wa}^d corresponds to droplet–solid and droplet–air interfacial areas. In State II, A_{wo} corresponds to the droplet–oil interfacial area. In State IV, A_{wo}^l and A_{wa}^l correspond to lens–oil and lens–air interfacial areas. (b) The regime map showing conditions where nucleation within the oil is preferred over nucleation in vapor for different ratios of γ_{wo}/γ_{wa}. (c) The regime map showing conditions where nucleation at the oil–air interface is preferred over nucleation at the solid–air interface for different solid surface wettabilities ($\theta_{ws(a)}$). (d) The regime map showing conditions where nucleation at the oil–air interface is preferred over nucleation within the oil for different surface wettabilities in oil ($\theta_{ws(o)}$). In (c) and (d), the region with a blue background corresponds to oils that satisfy the criterion $\gamma_{wo} \leq \gamma_{wa}$ while the region with a green background corresponds to oils with $\gamma_{wo} \geq \gamma_{wa}$.

Boltzmann constant, and E corresponds to the total interfacial energy of the cluster.[45] The number of molecules in the cluster n is related to the volume of the cluster as $n = V/v_m$ where v_m corresponds to the volume of a single molecule of condensate, $V = \pi\psi R^3/3$ is the volume of the cluster with a radius of curvature R and ψ is a shape factor associated with the geometry of the cluster. The interfacial energy term E can be expressed as

$$E = \psi\pi\left(\frac{3V}{\pi\psi}\right)^{2/3}\gamma = \psi\pi\left(\frac{3nv_m}{\pi\psi}\right)^{2/3}\gamma = n^{2/3}\beta \quad (1)$$

where, γ is the interfacial tension associated with the cluster and its environment. Thus the nucleation work function can be written as $W(n) = -n\alpha + n^{2/3}\beta$ where $\alpha = kT\ln(\text{SR})$ and $\beta = \psi\pi[(3v_m)/(\pi\psi)]^{2/3}\gamma$. By minimizing the nucleation work with respect to n, the work of formation ($W^* = 4\beta^3/27\alpha^2$) of a critical cluster size n^* (where $n^* = [(2\beta)/(3\alpha)]^3$) is obtained. Alternatively, the energy barrier for nucleation in each state can be evaluated through the critical supersaturation ($SR^* = \exp[(2\beta)/(3kTn^{*1/3})]$) required to cause nucleation of a critical cluster size n^*. The critical supersaturation SR^* required to form a critical cluster of size n^* is only dependent upon the surface energy (β and hence E) at a given temperature. By comparing the surface energies (E) in each state (see ESI Note 1†), we can determine a regime map of states that is favorable for nucleation.

Comparing State I and State III, the nucleation within oil is preferable if

$$\frac{E_{III}}{E_I} = \frac{\ln\left(SR_{III}^*\right)}{\ln\left(SR_I^*\right)} = \left(\frac{\psi_2}{\psi_1}\right)^{1/3}\frac{\gamma_{wo}}{\gamma_{wa}} < 1 \quad (2)$$

Here ψ is the shape factor of form $\psi = (2 + \cos\theta)(1 - \cos\theta)^2$. ψ_1 and ψ_2 are related to the contact angles of condensate in air ($\theta_{ws(a)}$) and oil ($\theta_{ws(o)}$), respectively, and lie in the limits of $0 \leq \{\psi_1, \psi_2\} \leq 4$. As a result even if the interfacial tension between a condensate and a liquid is less than the surface tension of condensate in air (i.e. $\gamma_{wo}/\gamma_{wa} < 1$), E_{III}/E_1 can be greater than one so that nucleation in the air environment may be more preferred compared to nucleation within a liquid, contrary to the hypothesis of Xiao et al.[25] At the same time, even if $\gamma_{wo}/\gamma_{wa} > 1$, nucleation within the liquid may be enhanced if the contact angle terms are such that eqn (2) is satisfied. The regime map satisfying eqn (2) is shown in Fig. 1b where the marked regions are the conditions under which nucleation in state III is more favourable than state I. A decrease in ratio of γ_{wo}/γ_{wa} can drastically decrease the actual energy barrier so that even non-wetting surfaces in an oil have smaller SR^* of nucleation compared to wetting surfaces in air (see ESI Fig. S2†). Substituting $\theta_{ws(o)} = 180°$ and $\theta_{ws(a)} = 90°$ for water in eqn (2), we find that $E_{III}/E_1 < 1$ for all oils with $\gamma_{wo}/\gamma_{wa} \leq 0.79$ (a condition met by most common oils with respect to water – see ESI Table 1† for examples), suggesting that homogeneous nucleation and thus by extension heterogeneous nucleation on any solid surface within such oils is favored than nucleation on a non-wetting surface in the air.

For the case when the oil does not cloak the condensate *i.e.* $S_{ow(a)} < 0$, and, the condensate does not wet the oil *i.e.* $S_{wo(a)} = \gamma_{oa} - \gamma_{wa} - \gamma_{wo} < 0$, nucleation at the oil–air interface (State IV) is preferable over nucleation at the solid–air interface (state I) if

$$\frac{E_{\mathrm{I}}}{E_{\mathrm{IV}}} = \frac{\ln\left(SR_{\mathrm{I}}^{*}\right)}{\ln\left(SR_{\mathrm{IV}}^{*}\right)} = \frac{\left(\psi_{1}\lambda^{2}\right)^{1/3}}{\xi}\frac{\sin\theta_{wo}}{\sin\theta_{wa}} > 1 \qquad (3)$$

where

$$\xi = \left(\frac{2}{1+\cos\theta_{wo}} - \cos\theta_{wo}\right) + \frac{\sin\theta_{wo}}{\sin\theta_{wa}}\left(\frac{2}{1+\cos\theta_{wa}} - \cos\theta_{wa}\right)$$

and $\lambda = \dfrac{\sin\theta_{wo}\left(2+\cos\theta_{wo}\right)}{\left(1+\cos\theta_{wo}\right)^{2}} + \dfrac{\sin\theta_{wa}\left(2+\cos\theta_{wa}\right)}{\left(1+\cos\theta_{wa}\right)^{2}}$

(see ESI Note 1†).

Similarly, nucleation at the oil–air interface (state IV) is preferable over nucleation at the solid–oil interface (State III) if

$$\frac{E_{\mathrm{III}}}{E_{\mathrm{IV}}} = \frac{\ln\left(SR_{\mathrm{III}}^{*}\right)}{\ln\left(SR_{\mathrm{IV}}^{*}\right)} = \frac{\left(\psi_{2}\lambda^{2}\right)^{1/3}}{\xi} > 1 \qquad (4)$$

In state IV, the two lens angles θ_{wa} and θ_{wo} are defined with respect to the plane of fluid and are bound by $\theta_{wo} + \theta_{wa} \leq 180°$. Here we consider the two cases that correlate the interfacial tensions at the contact line with the lens shape. For the first case, we consider oils with $\gamma_{wo}/\gamma_{wa} < 1$. Since $\gamma_{wo}\sin\theta_{wo} = \gamma_{wa}\sin\theta_{wa}$ from the force balance at the three phase contact line, this implies that for such oils $\theta_{wa} < \theta_{wo}$. Combined with the criterion $\theta_{wa} + \theta_{wo} \leq 180°$, this shows that for all oils with $\gamma_{wo}/\gamma_{wa} < 1$, the lens contact angle θ_{wo} is bound by $\{\theta_{wa} \leq \theta_{wo} \leq 180° - \theta_{wa}\}$ and $\max\{\theta_{wa}, \theta_{wo}\} = 90°$ Similarly, considering the second case when $\gamma_{wo}/\gamma_{wa} \geq 1$, the lens contact angle θ_{wa} is bound by $\{\theta_{wo} \leq \theta_{wa} \leq 180° - \theta_{wo}\}$. The regime maps satisfying eqn (3) and (4) are shown in Fig. 1c and d respectively. Also shown are regions corresponding to $\gamma_{wo} < \gamma_{wa}$ ($\theta_{wa} < \theta_{wo}$, blue), $\gamma_{wo} > \gamma_{wa}$ ($\theta_{wo} < \theta_{wa}$, green), and no-nucleation ($\theta_{wo} + \theta_{wa} > 180°$, grey). Clearly, condensation at the oil–air interface is always favorable when compared to nucleation on a perfectly non-wetting solid ($\theta_{ws(o)} = 180°$ or $\theta_{ws(a)} = 180°$) regardless of the environment. Fig. 1c shows that compared to hydrophobic surfaces in air, oils in which droplets remain largely immersed (*i.e.* oils with $\gamma_{wo} < \gamma_{wa}$) have lower energy barrier. The extent of such a lowering can even allow droplets to nucleate at significantly low supersaturation when compared to wetting solid surfaces in air (see ESI Fig. S3†). For oils with $\gamma_{wo} > \gamma_{wa}$, the number of combinations of $\theta_{wo} + \theta_{wa}$ that allow for nucleation enhancement are greatly restricted, mainly the oils with $\theta_{wa} < \theta_{ws(a)}$. On the other hand Fig. 1d shows that for oils with $\gamma_{wo} > \gamma_{wa}$, droplets that are largely immersed in air can nucleate more readily compared to nucleation within the oil. For such oils, nucleation can occur at very low supersaturations (see ESI Fig. S4†). In general, for oils with $\gamma_{wo} < \gamma_{wa}$, nucleation in state III is more favorable when compared to state IV if the condensate lens angle $\theta_{wo} > \theta_{ws(o)}$.

The preceding analysis is based on the assumption that the oil–air interface is atomically smooth. However, random thermal fluctuations can induce thermal-capillary waves, whose mean amplitude is expected[46] to be on the order of $(4\pi kT/\gamma)^{1/2} \approx 10$–$20$ Å for low surface tension oils ($\gamma < 30$ mN m^{-1}). Studies have shown that thermal capillary waves play an important role in the coalescence of droplets[47] and spreading of liquids.[48] The work of cluster formation at the oil–air interface could be lower than our estimate if we consider the dynamic roughness induced by such thermal-capillary waves; detailed study of these effects needs to be conducted and is out of scope of the present paper.

3.2 Nucleation dynamics in an immiscible oil

The framework for nucleation energy barrier developed in the preceding section can be used to determine the most preferred state for nucleation in different environments (oil or air). As an example, we find that on a LIS with hydrophobic solid surface, the energy barrier for nucleation of water in the presence of many oils is the highest in State I, and the lowest in State IV (see ESI Table 2 and Fig. S2–S4†). At the same time, as Fig. 1c and d show, nucleation within the oil (State II or III) can be favourable for many oil–solid combinations. However, a low nucleation energy barrier may not correspond to large nucleation rates, since the nucleation rate also depends on other factors such as nucleation site density, the diffusion coefficient of molecules and the sticking probability of molecules (also referred to as the accommodation coefficient) in an environment.[45] One may expect that very large supersaturation would be required in oils such as silicone oils or fluoropolymers (*e.g.* Krytox) that have low water miscibility to produce nucleation rates of similar magnitude as observed in air (see ESI Table 3† for a list of water solubilities in immiscible oils). Surprisingly, we find that under identical supersaturation, and assuming the accommodation coefficient as one, the nucleation rates within these oils can be of similar magnitude as the nucleation rates that can be obtained within air (see ESI Note 2†). The latter assumption however may be excessive for these oils. MD simulations show that the accommodation coefficient of water molecules on a water droplet covered with a monolayer of long chain organic alcohols could be substantially lower than one.[49] If the behaviour of water molecules in Silicone oils or Krytox is similar to their behaviour in the long chain organic liquids, then much higher supersaturation may indeed be required to nucleate a large number of droplets in these oils (see ESI Note 2†). However, a more fundamental question to ask is – can the vapor species become supersaturated in a liquid that is in contact with the condensing vapor upon subcooling.

The transport of a gaseous species through the liquid occurs by the sorption and diffusion mechanism.[50–52] According to Henry's Law, the maximum volume of vapor C_{s}, absorbed in a unit volume of liquid is given by $C_{s} = H_{v}P_{v}$ where H_{v} is Henry's constant of solubility of vapor in the liquid at a given temperature T_{v}, and P_{v} is the partial pressure of vapor above the liquid held at the same temperature as air.[52] Since the dissolution of gas in a liquid is an exothermic process,[53] the solubility limit of

vapor in liquids (and the Henry's Constant) is expected to increase when the temperature is decreased.[54,55] When a liquid is cooled to a temperature T_i (<the room temperature), then as long as condensation does not occur in air region near the subcooled liquid, the partial pressure of vapor near the liquid–air interface remains unaffected. Since the total pressure remains the same (equal to absolute pressure), the maximum amount of vapor that can get absorbed is $C_{s,i} = H_i P_v$ where H_i (>H_v) is the Henry's constant at temperature T_i. Thus, as the liquid is cooled, it becomes under-saturated. The liquid absorbs more vapor due to increased solubility but only till its new solubility limit. Consequently, the vapour cannot supersaturate within the liquid and droplet formation by condensation cannot occur.

To validate this aspect, we conducted a series of experiments. In the first experiment, we lowered the temperature of a liquid below the room-temperature to ascertain if condensation occurs within the oil (see Methods). To prevent supersaturation in the air near the setup, the temperature was maintained above the dew point in air (Peltier temperature: 16 ± 1 °C, Dew Point: 13 ± 1 °C). Silicone oil of viscosity 10 cSt was chosen as a test liquid because of its low vapor pressure. Despite exposing the oil to the humid environment (room humidity of 47%) for two hours, no trace of condensation was observed within the oil (Fig. 2a). Condensation however proceeded immediately when the temperature was lowered below the dew point in air (Fig. 2b) and microscopic droplets were identified at the optical plane near the oil–air interface.

In the second experiment, we performed a more rigorous test to determine if water drops can condense within the oil in the complete absence of the oil–air interface by lowering its temperature substantially. A 10 cc glass vial was completely filled with a solution of 10 cSt silicone oil saturated with moisture (see Methods and ESI Fig. S1† for the schematic of the setup). The vial was wrapped with insulation and cooled to -2 °C using a peltier cooler for a period of three hours. To detect the formation of nanoscale drop formation within the oil, we performed dynamic light scattering (DLS) measurements on the solution samples extracted from the vial within 30 minutes of taking the vial off the peltier cooler. The DLS instrument used

in the study had a minimum detection size of 0.2 nm in hydrodynamic radius. We performed multiple measurements over different volumes of the solution, however the DLS measurements showed a complete absence of any droplet formation within the oil.

Based on the above results, it is unlikely that nucleation can occur within the bulk oil. Our observations suggest that the formation of droplets on the bulk silicone oil is directly linked with the saturation dynamics in air. In the case of a subcooled oil exposed to air, the region of supersaturation lies in the air beyond the oil–air interface and hence nucleation of a droplet is likely to occur at the oil–air interface, irrespective of the nature of oil.

3.3 State of the droplet on spreading oils after-nucleation: cloaked or uncloaked?

Having established that the nucleation is most likely to occur at the oil–air interface, we now investigate the dynamics during the droplet growth process, especially on oils that cloak the condensates. Post-nucleation, the growth of a droplet at the oil–air interface on a non-cloaking oil can readily occur through direct diffusion of the vapor to the drop surface.[40] For droplets growing at the oil–air interface on spreading oils, a layer of the oil might be introduced between the vapor and the drop if the rate of droplet growth (U_d) is lower than the spreading rate of oil on the condensing droplet (U_s). In the opposite case, the drop surface will be exposed and the condensation on spreading oil can be expected to behave similar to condensation on non-spreading oil or a solid surface.

The growth of droplets is influenced by several factors such as droplet density, saturation conditions *etc.*[1,43,56] To estimate droplet growth rate (U_d), we consider the growth of an isolated droplet at the oil–air interface. We assume that the droplet at the oil–air interface has a lens shape, and the droplet and the oil are at temperature T_i. With these assumptions, the droplet growth law is given by $R = \varphi^{1/3}\sqrt{2\eta t}$ where R is the radius of curvature of the upper segment of the lens, φ is a geometric factor that relates the volume change of the lens with condensation at the lens-air interface. The detailed derivation of our model is provided in the ESI Note 3.† The droplet growth rate ($U_d = dR/dt$) is given by

$$U_d = \varphi^{1/3}\sqrt{\frac{\eta}{2t}} \tag{5}$$

where

$$\eta = \frac{4M_w D_{ab} P_{i0} SR}{\rho_w \psi_{wa} \overline{R} T_i}\left(\frac{T_i}{T_v} - \frac{1}{SR}\right) \text{ and } \varphi^{-1} = 1 + \frac{\psi_{wo}}{\psi_{wa}}\left(\frac{\sin\theta_{wa}}{\sin\theta_{wo}}\right)^3$$

Here M_w, ρ_w, D_{ab}, SR, T_v, T_i, P_{i0}, $\overline{R}$ denote the molecular weight of the condensate, density of the condensate, diffusion coefficient of vapor in air, saturation ratio, vapor temperature, droplet temperature, saturation vapor pressure at temperature T_i, and gas constant, respectively. $\psi_{wo} = (2 + \cos\theta_{wo})(1 - \cos\theta_{wo})^2$ and $\psi_{wa} = (2 + \cos\theta_{wa})(1 - \cos\theta_{wa})^2$ are the shape factors of the lower and upper segment of the lens (Fig. 1a, State
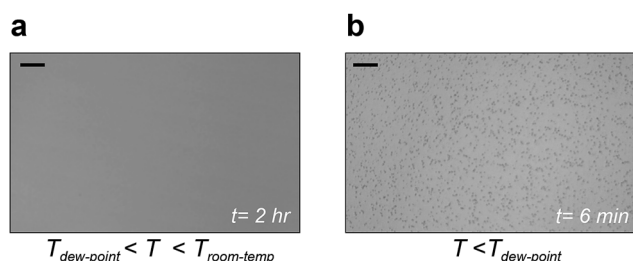

a $t = 2$ hr

$T_{dew-point} < T < T_{room-temp}$

b $t = 6$ min

$T < T_{dew-point}$

Fig. 2 Condensation at the liquid–air interface (a). Representative image showing no observable condensation after two hours within the liquid when the liquid temperature is greater than dew point ($T_{dew-point}$) but less than room temperature ($T_{room-temp}$). (b) Representative image showing condensation at the liquid–air interface when the temperature is reduced below the dew point. Scale bars represent 20 μm. For the complete video, see ESI movie S1.†

IV). Having estimated the growth rate of droplets, we now consider the spreading rate of the oil on the droplet. The spreading of oil on a drop can be delineated into two stages. During the first stage, a monolayer driven by balance between surface tension gradient and shear stress at the oil-droplet interface spreads on the droplet.[57] For the radial spreading of an oil monolayer on water, it has been shown that the spreading front location follows Joos law[57] and is given by $R_{s,m} = \sqrt{4S_{ow(a)}/3\sqrt{\mu_o\rho_o}}t^{3/4}$ from where the spreading velocity is found as $U_{s,m} = \sqrt{3S_{ow(a)}/4\sqrt{\mu_o\rho_o}}t^{-1/4}$. Here ρ_o, μ_o denote the density and dynamic viscosity of the oil and $S_{ow(a)}$ is the spreading coefficient of oil on water as measured in air. Although the spreading of oil around a droplet is expected to be greater compared to spreading of oil in a plane, the latter can be used as an approximation for the spreading velocity around a droplet. The monolayer is followed by a nanofilm with thickness up to few hundred nanometers.[58] The spreading rate of this nanofilm is dictated by the capillary forces opposed either by inertial or viscous forces. To determine the predominant dissipating force during this spreading regime, we consider the Ohnesorge number ($Oh = \mu_o/\sqrt{\rho_o R\gamma_{oa}}$) of the oil with the characteristic length of the droplet radius.[58] For water droplets of size <100 nm on Silicone oil of viscosity 10 cSt and above, we find that $Oh > 1$, implying that the spreading of oil on droplets during growth occurs in the viscous regime. In a recent work, Carlson et al.[58] have shown that for an oil spreading on a droplet in the viscous regime, the spreading front location $R_{s,\mu}$ follows $R_{s,\mu} \approx 0.87R(\gamma_{wo}t/\mu_o R)^{0.3}$ from where the spreading velocity on a growing droplet is given by $U_{s,\mu} \approx 0.72\eta^{0.35}(\gamma_{wo}/\mu_o)^{0.3}t^{-0.35}$.

Knowing the droplet growth rate and cloaking rates of the monolayer and nanofilm, we can now establish if droplets remain cloaked or not during the growth process. Comparing the droplet growth rate with the monolayer cloaking rate, we find $U_{s,m}/U_d \sim k_m t^{0.25}$ where $k_m = \sqrt{3S_{ow(a)}/2\varphi^{2/3}\eta\sqrt{\mu_o\rho_o}}$. Depending upon the value of the pre-factor k_m, the droplet may remain uncloaked for a time $t_{uncloak}$ during which $U_{s,m}/U_d \sim k_m t^{0.25} < 1$. For a water nanodroplet on silicone oil of viscosity 1000 cSt, substituting the relevant values ($S_{ow(a)} = 5$ mN m^{-1}, $\rho_o = 970$ kg m^{-3}, $\rho_w = 980$ kg m^{-3}, $T_v = 293$ K, and $D_{ab} = 2 \times 10^{-5}$ m^2 s^{-1}) we find that depending upon the lens angles ($0 < \theta_{wa}, \theta_{wo} < 180°$ and $\theta_{wa} + \theta_{wo} \leq 180°$ since the θ_{wa}, θ_{wo} are unknown) and supersaturation (SR), the constant $k_m \sim 10^1$–10^4 from which the $t_{uncloak}$ can be estimated to be between 10^{-16}–10^{-4} s. The large values of $t_{uncloak}$ are obtained for large supersaturation ($T_v - T_i = 20$ K) and for very small lens angles ($\theta_{wa}, \theta_{wo} < 10°$).

Next, comparing the droplet growth rate with the spreading rate of the nanofilm, we find $U_{s,\mu}/U_d \sim k_\mu t^{0.15}$ where $k_\mu = 1.02\varphi^{-0.1}(\gamma_{wo}^2/\eta\mu_o^2)^{0.15}$. Since $U_{s,\mu}/U_d \sim t^{0.15}$, the spreading of nanofilm will overcome the droplet growth eventually. By substituting the relevant values for the water nanodroplet on Silicone oil we find that depending upon the lens angles and supersaturation ratios, the time taken by the thicker sub-microscopic film to form around the growing droplet lies in the range of 10^{-9}–10^{-3} s. Based on above calculations, we conclude that after a tiny fraction of time,

the condensing droplets on a cloaking oil are cloaked by the oil nanofilm.

Although, visualization of nanodroplet formation and the cloaking process during the initial droplet growth is challenging, the evidence for the last statement can be obtained by indirect experimental observations. An oil film cloaking a droplet would tend to submerge the droplet within the oil in order to minimize its own surface energy. As a consequence, condensed droplets are expected to be located in the oil in a fully submerged state. Results from the optical microscopy (Fig. 2b) indicate the presence of droplets near the oil–air interface; however, the exact location of the droplets could not be determined because of limits in spatial resolution of the microscope. Recently, Rykaczewski et al.[36] developed a technique that can reveal nanoscale details of the underlying structure of droplets and substrate interfaces. Using this technique, we obtained direct cross-sectional images of the topography beneath the 1000 cSt and 10 cSt silicone oil surfaces up to a depth of 10–20 μm, after condensing vapor on them under the same conditions (see Methods). The regions on the oil surfaces for obtaining the cross-sectional images were selected randomly. By visualizing the Cryo-SEM images using the backscattered detector, the water and oil phases were separately identified (see Methods for an extended description on phase identification). Images in Fig. 3a–d show the morphology of 1000 cSt and 10 cSt silicone oil surfaces with condensed
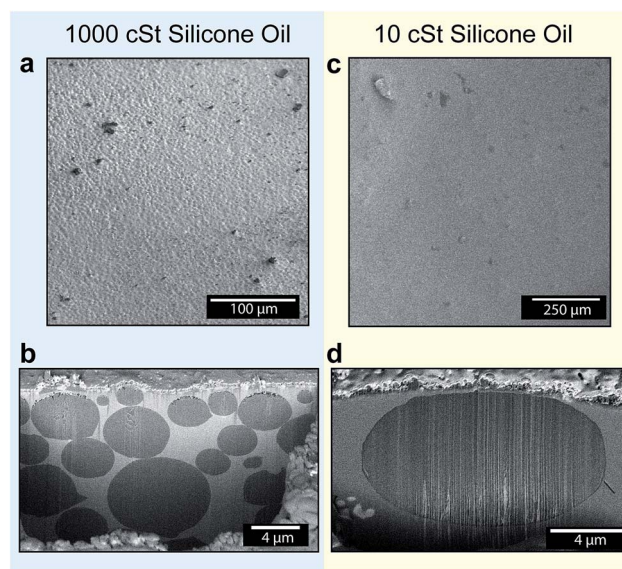
Fig. 3 Visualization of submerged droplets (a). 1000 cSt silicone oil surface with condensed droplets as observed in SEM. The sample was prepared using the Cryo-FIB-SEM technique where condensed water micro-droplets and the liquid surface are cryopreserved in a vitreous state and subsequently milled using an ion beam and imaged using an electron-beam. (b) Cross-sectional view of the cryo-FIB sectioned surface of 1000 cSt oil showing the presence of droplets within the oil in different depths. (c) 10 cSt Silicone oil surface as observed in SEM before sectioning. (d) Cross-sectional view of the cryo-FIB sectioned surface of 10cst oil showing the presence of a single droplet near the oil–air interface. The droplet appears ellipsoidal because the sample is inclined by 52°.

droplets before and after sectioning. The cross-sectional images of the 1000 cSt and 10 cSt silicone oil surfaces (Fig. 3b and d) clearly show the presence of fully submerged droplets (dark grey in color) within the oils (light grey in color), thereby confirming the previously predicted behaviour of droplets condensing on the cloaking liquid.

From the images obtained using Cryo-FIB-SEM (Fig. 3), several other insights into the droplet growth mechanics can be drawn. Fig. 3a shows that prior to the sectioning of the 1000 cSt Silicone oil surface, the surface appeared rough with microscale features emerging out of the oil. The cross-section of the 1000 cSt oil surface (Fig. 3b) shows the presence of uneven size droplets arranged in stacks within the oil. The stacking of the droplets leads to deformation of the oil–air interface, giving rise to the appearance of roughness observed in Fig. 3a. The droplets also appear to be densely packed, with less than 100 nm separations between many neighboring droplets (see Fig. S5–S6† for more examples). In comparison with the condensation pattern on the 1000 cSt silicone oil surface, the oil–air interface of the 10 cSt silicone oil surface appeared to be relatively smoother (Fig. 3c). The cross-sectional image of the selected region showed the presence of a single fully submerged droplet within the oil (Fig. 3d). The apparent difference in the submerged droplet sizes in similar volumes of the two oils is attributed to the different viscosities of the oils that affect the coalescence behaviour of the droplets.

Based on the results and arguments mentioned above, the nucleation and submergence mechanism on cloaking oils is proposed to occur in the following steps (Fig. 4): (a) a droplet nucleates at the oil–air interface, (b) subsequently, the droplet is cloaked by the oil, (c) the cloaking leads to submergence of the droplet within the oil due to capillary forces, thereby creating a fresh oil–air interface, and (d) finally, the cycle (a)-(c) is repeated with new generation of droplets forming at the oil–interface and submerging. The interaction between the old and the new generation of droplets may lead to re-organization of droplets. Depending upon the oil viscosity, it may result in different arrangements within the oil (such as stacked arrangements as

observed in Fig. 3b, or a single droplet Fig. 3d). A more detailed examination of this aspect will be performed at the later part of this work.

The preceding discussion relates to the fate of droplets whose size is smaller than the oil thickness surrounding them. But even if the droplet size becomes larger than the oil thickness surrounding it, the droplet still remains cloaked as it grows. The local equilibrium thickness of the cloak profile around such droplets is dependent upon the balance between spreading forces (due to repulsive Van der Waal's interaction between oil and vapor) that tend to thicken the cloak around the droplet, and the positive pressure gradient developed in the film due to difference in disjoining pressure and the hydrodynamic pressure that tends to thin down the cloak. Formation of the cloaked film on a droplet can occur with a minimal contact between the spreading oil and a droplet, e.g. for a droplet suspended on a LIS.[20,58] To directly visualize the presence of such a cloaked film, we used the cryo-FIB-SEM technique to obtain a cross-section of a randomly selected condensed droplet with size larger than the post-spacing on 10 cSt Silicone oil LIS (Fig. 5). Although the oil cloak thickness may be a function of time, oil properties, droplet size etc., Fig. 5 provides a general representation of the cloak profile around the droplet. The images show that the cloak profile around the droplet decreases sharply beyond the wetting ridge height. The thickness profile was estimated at ~65 nm around the droplet and remains mostly uniform around the droplet. Surprisingly, we find a thicker oil profile near the apex of the droplet. A closer inspection of this region shows the presence of two sub-microscopic droplets with a diameter of ~100 nm and 250 nm within the oil film (a magnified image on top of Fig. 5, and ESI Fig. S11† provided separately). It is likely that these droplets nucleated on the oil cloak and the tendency of the oil to form the cloak around these droplets provided the driving force to cause oil imbibition that resulted in the thickening of the oil cloak.

As evident from the observations of Fig. 2 and 5 and condensation on cloaking liquids in prior studies, the growth of nanoscopic droplets to larger sizes occurs despite the complete engulfment of the droplets by the oil. In the next sections, we discuss the mechanisms of droplet growth on the cloaking liquids.

3.4 Droplet growth: the role of permeation

It is well known that the growth of droplets on surfaces occurs via either direct vapor accretion at the droplet surface, or via coalescence with neighbouring droplets. For droplet growth on a cloaking liquid, the first mechanism is improbable because the oil film acts as a barrier against direct diffusion of vapor molecules to the droplet surface. Despite the oil layer acting as the barrier, vapor molecules can permeate through the film in the presence of concentration gradient across the film.

However, the role of permeation and diffusion in the growth of a droplet submerged within the oil is unclear. A droplet of radius R immersed within the oil has excess pressure due to its curvature, and as a result, the chemical potential of the
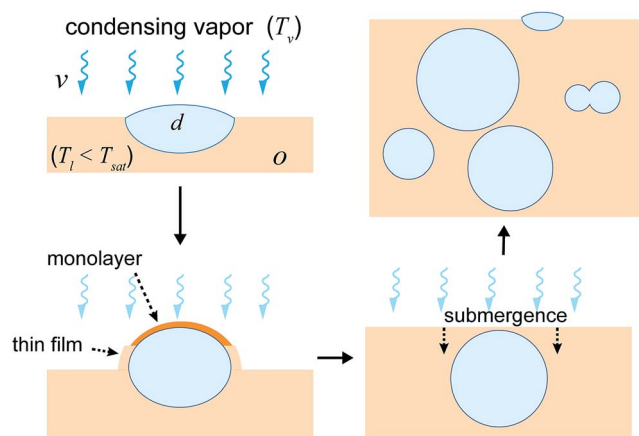

Fig. 4 Schematic of the droplet nucleation and submergence mechanism on cloaking liquids.
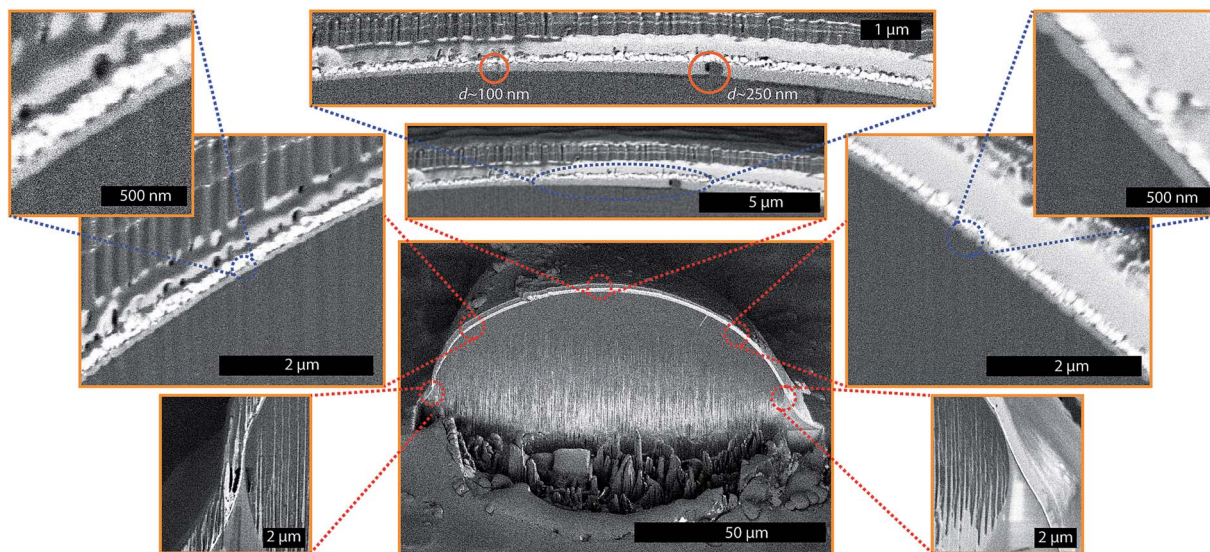
Fig. 5 Nanofilm profile around a condensed droplet suspended on LIS. The liquid film profile around the droplet (droplet size > micropost spacing) on 10 cSt silicone oil obtained through the Cryo-FIB-SEM process. The micropost surface was OTS coated silicon samples with micropost arrays ($a = b = h = 10$ μm, where a is the post width, b is the edge-to-edge spacing between posts and h is height of the posts). The light grey color in the images sandwiched between the dark grey (water) and white (platinum) signifies Silicone oil of viscosity 10 cSt. Different sections around the droplet were imaged separately after milling the droplet. The higher magnification images are overlapped on the image of the entire droplet as an aid for visualization. Within the liquid cloak, the presence of two separate nano-droplets is noticeable. Because of the sample tilt, and its position with respect to the detector, different sections of the droplet are located at different depths of focus, thus giving different contrast. For this reason, the left section of the droplet profile looks darker while the right section of the droplet profile looks evenly bright, even though the entire surface is coated with the same chemical (Platinum). The image content beyond edge of the cross-section (above edge of Pt coating) is out-of-focus with each pixel signal coming from a broad volume and is meaningless. A full-scale image of the nano-droplets within the cloak can also be visualized through ESI Image S11.†

dispersed phase at the droplet surface and in the bulk are different. From the Kelvin equation, the concentration of molecules (C_r) around a droplet is given by[59] $C_r = C_s \exp[(2\gamma_{wo})/(\rho_w R\bar{R}T)]$. Here, C_s is the bulk phase solubility and ρ_w is the density of the dispersed phase (water). Thus the concentration of dispersed phase molecules around the droplet is higher than the concentration within the oil. For droplet growth to occur within the oil, the solute (vapor here) content within the oil must exceed C_r. However as described in the preceding section, the vapor saturation in the oil is limited by the sorption mechanism and this makes it unlikely for vapor to achieve supersaturation in the oil. Even if the oil layer thickness is sub-microscopic, the solute transport across the film is governed by the sorption mechanism (*e.g.*, in studies on coarsening of the foams, the gas permeation across the thin lamellae is described using this mechanism,[60,61] see ESI Note 3† for more discussion on this aspect). Based on above arguments, droplet growth through permeation of vapor molecules in the oil appears unlikely.

Despite the limits on the vapor content within oil due to sorption, vapor supersaturation within the oil may be possible *via* other mechanisms. As an example, the presence of nucleated droplets at the oil–air interface can alter the solute content within the oil. In the previous paragraph it was explained that because of the droplets' curvature, the droplet surface has excess solute concentration compared to the bulk solubility limit. If the oil is under-saturated, then the droplet dissolves with diffusion within the oil acting as the rate-limiting step. In general, this mechanism could result in the increase of

supersaturation within the oil that may result in heterogeneous or homogeneous nucleation within the oil or act as the source of growth of other droplets. However, identifying the contribution of vapor diffusion within the oil to the overall growth of a submerged droplet is difficult because of several reasons. First, the nucleation rate at the oil–air interface is difficult to estimate precisely. Secondly, the percentage and size of the nucleated droplets that may dissolve is unknown. As a result, it is challenging to estimate the supersaturation within the oil layer due to droplet dissolution.

3.5 Droplet growth: the role of oil viscosity and coalescence

The difference in droplet sizes is observed through cryo-FIB-SEM (Fig. 3a–d) and the presence of droplets within the oil cloak (Fig. 5) is attributed to the presence of the intervening oil film around the droplets, and its effect on delaying coalescence. The process of coalescence in the presence of an outer viscous fluid occurs in two stages.[62] During the first stage, the oil drains from in-between two droplets thereby bringing them into sufficient proximity so that small instability propagating on the droplet surface can cause a capillary bridge formation. Once the two droplets are in contact, the bridge expands to achieve a minimal energy state.[63–66]

The dynamics of coalescence between two neighbouring droplets at an interface during condensation is a complex function of their size, growth rate of droplets, and attractive forces due to capillary interactions between them. Solving for

the complete drainage between condensing droplets is beyond the scope of this work. However using the Stefan Reynolds Flat plate model,[64,66] we find that when the droplets are separated by distances where the drainage happens purely to van der Waals forces, the drainage time is directly proportional to oil viscosity (see ESI Note 4†). The delay in coalescence of macroscopic droplets placed in each others vicinity (∼mm) on LIS due to decreased drainage rates in the case of higher viscosity oil has recently been also confirmed.[67]

We thus expect the viscosity of the oil to have a significant effect on growth of droplets during condensation. Previous studies on breath-figure formation on polymer–solvent mixtures[68] have also hinted towards its importance, however the use of solvent alters the solution viscosity and masks the true effect of the oil viscosity on condensation. To observe this effect, we performed condensation experiments on LIS prepared by impregnating OTS coated microtextured surface with silicone oils of viscosity of 10, 100 and 1000 cSt (see Methods). The impregnation of the OTS coated surface with silicone oils results in complete submergence of solid (including post-tops)

in the presence of air and water.[20] Upon condensation, we notice the formation of darkened regions (as a result of droplets nucleating on the post-tops) and their subsequent disappearance (owing to their getting pulled within the oil spacing due to capillary forces originating from the Laplace pressure of the oil cloak around the droplet). As a result of submergence of such droplets and of droplets nucleating on oil itself, the water droplets displace the oil resulting in the oil draining out of the LIS and flooding the surface. However, as the size of the submerged droplets exceeds the post-spacing, they can transition to the post-tops and the oil can flow back within the texture to fill in the void left behind. For low viscosity oil cases (10 cSt and 100 cSt LIS) the oil displacement appears less severe compared to the 1000 cSt LIS because in the former cases, the oil can drain quickly between the submerged droplets allowing them to coalesce more rapidly and grow at a faster rate. On 1000 cSt LIS, significant suppression of condensation growth is observed that we postulate is due to the increased drainage time and higher oil content around the droplets caused by the oil displaced from within the texture (Fig. 6a–c, also see ESI Movie
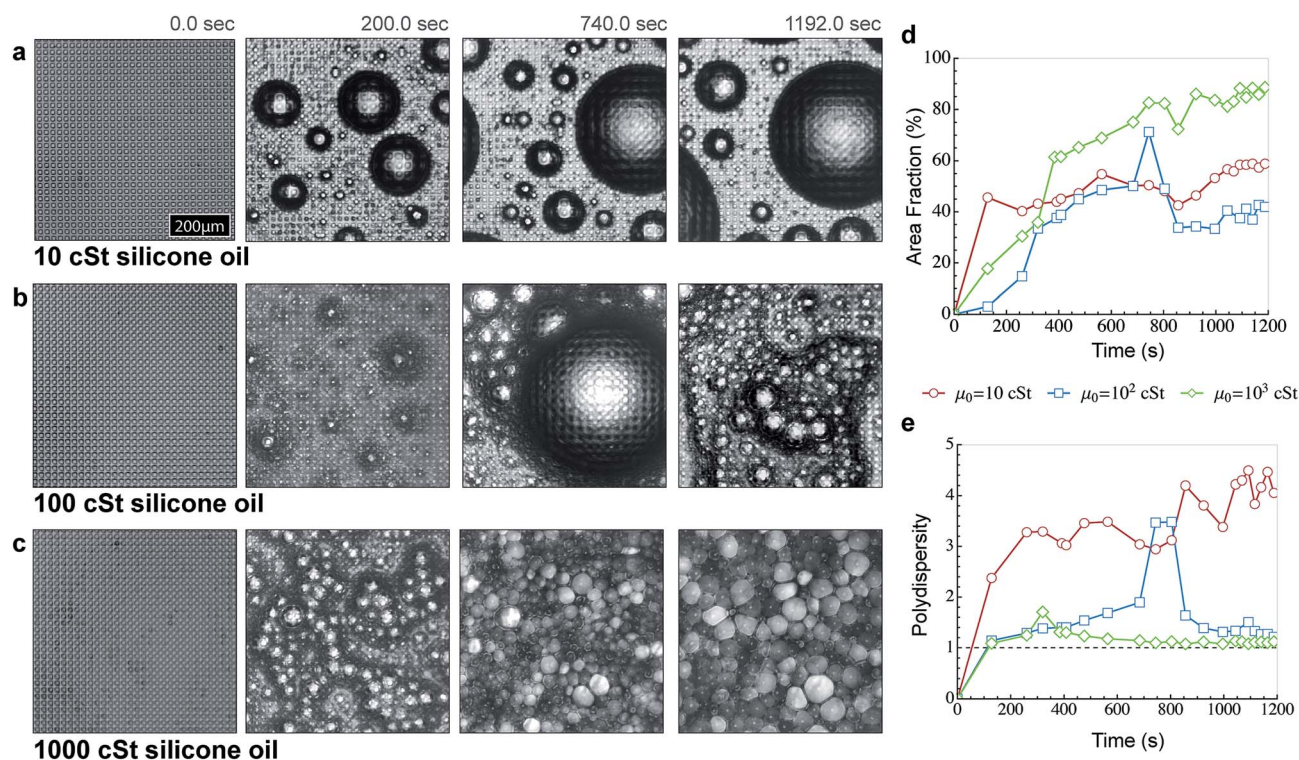

Fig. 6 Effect of liquid viscosity during condensation on LIS. (a) Time sequence showing growth of condensed droplets as observed under a microscope on the micropost surface (identical surfaces are used in Fig. 5) impregnated with Silicone oil of viscosity (a) 10 cSt, (b) 100 cSt and (c) 1000 cSt. The experiments were performed in an open environment under the same conditions (Peltier temperature = 3 ± 1 °C and dew point = 12 ± 1 °C). Even on 100 cSt, significant resistance to coalescence is observed. On the 1000 cSt Silicone oil surface, there is significant inhibition against coalescence and condensed droplets are separated through a thin oil film that takes orders of magnitude larger time to collapse as compared to droplets cloaked with 10 and 100 cSt viscosity silicone oil. (d) Plot comparing the variation of the droplet occupied area fraction versus time on 10, 100 and 1000 cSt silicone oil impregnated surfaces. On the 10 cSt surface, the droplet coverage reaches ∼55% as is normally observed on condensation on solid surfaces. On the 100 cSt surface, there is an initial delay in forming of large droplets within the observed frame, but large size droplets are formed and move out of frame due to coalescence events. In comparison, the droplet coverage reaches ∼90% within minutes on the 1000 cSt surface. (e) Plot comparing the variation of droplet sizes (polydispersity) versus time on 10, 100 and 1000 cSt Silicone oil impregnated surfaces. The actual polydispersity and area coverage on 100 cSt was significantly higher, but the spatial resolution limits prohibited identification of individual droplets from the background.

S3†). To quantify the difference in growth behaviour, we obtained droplet coverage over time (Fig. 6d) and the poly-dispersity in size distribution over these surfaces (Fig. 6e, see Methods). From Fig. 6d, it is evident that the fraction of surface area occupied by the droplets increases continuously across all the three samples. On 10 cSt LIS, the droplet area fraction rapidly reaches a coverage close to 50–55%, similar to the average area fraction[1] observed during condensation on solid surfaces. Although the droplets are cloaked, but the drainage of oil between the droplets is more efficient due to which the drops can coalesce rapidly, thus leaving a large fraction of the surface unoccupied by the droplets. This is also evident from the polydispersity graph (Fig. 6e), where it can be seen that droplet sizes on 10 cSt LIS become increasingly polydisperse with time. The image analysis of 100 cSt LIS was less accurate because the droplet growth behavior on this surface made it difficult to identify the droplet boundaries. Although the area coverage on 100 cSt LIS shows similar trends as observed on 10 cSt LIS, the actual coverage was larger.

On the 1000 cSt surface, a fascinating range of droplet growth behavior with several distinctive features was observed. First, after a short duration, the polydispersity in size distribution vanished and a very narrow size-distribution of droplets was obtained. Second, significant inhibition against coalescence was observed; yet the droplet size increased with the passage of time evidenced by the continuous increase in droplet coverage over the surface (Fig. 6d). Third, the droplet shape changed from spherical to polyhedral with time and condensed droplets appear to self-assemble in closely packed honeycomb like structures (Fig. 6c). Initially, the condensation pattern was reminiscent of wet foam architecture, while at later times the condensation pattern resembled dry foam architecture. The polyhedral droplet profiles are separated through thin films resembling plateau borders and intersect at ~120° as dictated by the equilibrium requirement for three equal surface tension forces at intersection[69] (also see ESI Fig. S7†). Finally, the focal plane of the microscope constantly needed to be raised to keep a sharp focus on the droplets, implying that multiple layers of stacked droplets were being formed.

4. Conclusions

In summary, we have examined the detailed mechanics underlying the droplet formation and subsequent growth processes on liquids. By examining at the energetics of the nucleation process, we have provided regime maps that can guide the selection of liquids that enhance nucleation rates at lower supersaturation. Here we find that the vapor content within the liquid is limited by the sorption mechanics, so that nucleation on subcooled liquid is most likely to occur at the liquid–air interface. By investigating the spreading rates of cloaking liquids and the condensate growth rate, we have provided a mechanistic understanding of the process that leads to submergence of droplets that nucleate at the liquid–air interface. While the submergence of condensing droplets within the cloaking liquids maybe useful in some applications (such as breath-figure templating); for the application of LIS in

condensation, it can potentially decrease the longevity of the coating by displacing the impregnated liquid out of the texture. For the first time, we provide a direct visualization of the nanoscale liquid film profile around a droplet and show that sub-microscopic droplets can nucleate on the liquid cloak itself. Finally, by doing a systematic study of condensation on different viscosity oils, we have uncovered the role of oil viscosity in governing the droplet growth behaviour.

Acknowledgements

References

1 D. Beysens, *Atmos. Res.*, 1995, **39**, 215–237.
2 W. M. Rohsenow, J. P. Hartnett and Y. I. Cho, *Handbook of heat transfer*, McGraw-Hill, New York, 1998.
3 J. W. Rose, *Proc. Inst. Mech. Eng., Part A*, 2002, **216**, 115–128.
4 V. P. Carey, *Liquid-vapor phase-change phenomena*, Taylor & Francis, New York, 2007.
5 C. Dietz, K. Rykaczewski, A. G. Fedorov and Y. Joshi, *Appl. Phys. Lett.*, 2010, **97**, 033104.
6 A. T. Paxson, J. L. Yagüe, K. K. Gleason and K. K. Varanasi, *Adv. Mater.*, 2014, **26**, 418–423.
7 R. D. Narhe and D. A. Beysens, *Phys. Rev. Lett.*, 2004, **93**, 076103.
8 D. Torresin, M. K. Tiwari, D. Del Col and D. Poulikakos, *Langmuir*, 2013, **29**, 840–848.
9 G. Azimi, R. Dhiman, H. M. Kwon, A. T. Paxson and K. K. Varanasi, *Nat. Mater.*, 2013, **12**, 315–320.
10 J. B. Boreyko and C. H. Chen, *Phys. Rev. Lett.*, 2009, **103**, 184501.
11 X. Chen, J. Wu, R. Ma, M. Hua, N. Koratkar, S. Yao and Z. Wang, *Adv. Funct. Mater.*, 2011, **21**, 4617–4623.
12 N. Miljkovic, R. Enright and E. N. Wang, *ACS Nano*, 2012, **6**, 1776–1785.
13 C. Dorrer and J. Rühe, *Langmuir*, 2007, **23**, 3820–3824.
14 Y. C. Jung and B. Bhushan, *J. Microsc.*, 2008, **229**, 127–140.
15 K. K. Varanasi, M. Hsu, N. Bhate, W. Yang and T. Deng, *Appl. Phys. Lett.*, 2009, **95**, 094101.
16 D. Quéré, *Rep. Prog. Phys.*, 2005, **68**, 2495–2532.
17 T. S. Wong, S. H. Kang, S. K. Y. Tang, E. J. Smythe, B. D. Hatton, A. Grinthal and J. Aizenberg, *Nature*, 2011, **477**, 443–447.
18 A. Lafuma and D. Quéré, *EPL*, 2011, **96**, 56001.
19 S. Anand, A. T. Paxson, R. Dhiman, J. D. Smith and K. K. Varanasi, *ACS Nano*, 2012, **6**, 10122–10129.
20 J. D. Smith, R. Dhiman, S. Anand, E. Reza-Garduno, R. E. Cohen, G. H. McKinley and K. K. Varanasi, *Soft Matter*, 2013, **9**, 1772–1780.

21 K. Rykaczewski, A. T. Paxson, M. Staymates, M. L. Walker, X. Sun, S. Anand, S. Srinivasan, G. H. McKinley, J. Chinn, J. H. J. Scott and K. K. Varanasi, *Sci. Rep.*, 2014, **4**, 4158.

22 X. Yao, Y. Hu, A. Grinthal, T. S. Wong, L. Mahadevan and J. Aizenberg, *Nat. Mater.*, 2013, **12**, 529–534.

23 H. J. J. Verheijen and M. W. J. Prins, *Langmuir*, 1999, **15**, 6616–6620.

24 T. Krupenkin, S. Yang and P. Mach, *Appl. Phys. Lett.*, 2003, **82**, 316–318.

25 R. Xiao, N. Miljkovic, R. Enright and E. N. Wang, *Sci. Rep.*, 2013, **3**, 1988.

26 A. V. Limaye, R. D. Narhe, A. M. Dhote and S. B. Ogale, *Phys. Rev. Lett.*, 1996, **76**, 3762–3765.

27 G. Widawski, M. Rawiso and B. François, *Nature*, 1994, **369**, 387–389.

28 O. Karthaus, N. Maruyama, X. Cieren, M. Shimomura, H. Hasegawa and T. Hashimoto, *Langmuir*, 2000, **16**, 6071–6076.

29 M. Srinivasarao, D. Collings, A. Philips and S. Patel, *Science*, 2001, **292**, 79–83.

30 R. Takekoh and T. P. Russell, *Adv. Funct. Mater.*, 2014, **24**, 1483–1489.

31 A. Bolognesi, C. Mercogliano, S. Yunus, M. Civardi, D. Comoretto and A. Turturro, *Langmuir*, 2005, **21**, 3480–3485.

32 M. Voigt, S. Dorsfeld, A. Volz and M. Sokolowski, *Phys. Rev. Lett.*, 2003, **91**, 026103.

33 J. Bruining and D. Marchesin, *Phys. Rev. E: Stat., Nonlinear, Soft Matter Phys.*, 2007, **75**, 036312.

34 A. R. Kovscek, *J. Pet. Sci. Eng.*, 2012, **98–99**, 130–143.

35 J. Seiwert, C. Clanet and D. Quéré, *J. Fluid Mech.*, 2011, **669**, 55–63.

36 K. Rykaczewski, T. Landin, M. L. Walker, J. H. J. Scott and K. K. Varanasi, *ACS Nano*, 2012, **6**, 9326–9334.

37 K. Rykaczewski, S. Anand, S. B. Subramanyam and K. K. Varanasi, *Langmuir*, 2013, **29**, 5230–5238.

38 S. B. Subramanyam, K. Rykaczewski and K. K. Varanasi, *Langmuir*, 2013, **29**, 13414–13418.

39 M. D. Abràmoff, P. J. Magalhães and S. J. Ram, *Biophotonics International*, 2004, **11**, 36–41.

40 C. M. Knobler and D. Beysens, *Europhys. Lett.*, 1988, **6**, 707–712.

41 A. Scheludko, V. Chakarov and B. Toshev, *J. Colloid Interface Sci.*, 1981, **82**, 83–92.

42 A. D. Alexandrov, B. V. Toshev and A. D. Scheludko, *Colloids Surf., A*, 1993, **79**, 43–50.

43 A. A. Nepomnyashchy, A. A. Golovin, A. E. Tikhomirova and V. A. Volpert, *Phys. Rev. E: Stat., Nonlinear, Soft Matter Phys.*, 2006, **74**, 021605.

44 F. Eslami and J. A. W. Elliott, *J. Phys. Chem. B*, 2011, **115**, 10646–10653.

45 D. Kashchiev, *Nucleation*, Butterworth-Heinemann, 2000.

46 F. P. Buff, R. A. Lovett and F. H. Stillinger Jr, *Phys. Rev. Lett.*, 1965, **15**, 621–623.

47 D. G. Aarts, M. Schmidt and H. N. Lekkerkerker, *Science*, 2004, **304**, 847–850.

48 B. Davidovitch, E. Moro and H. A. Stone, *Phys. Rev. Lett.*, 2005, **95**, 244505.

49 S. Sakaguchi and A. Morita, *J. Chem. Phys.*, 2012, **137**, 064701.

50 R. M. Barrer and E. K. Rideal, *Trans. Faraday Soc.*, 1939, **35**, 628–643.

51 J. G. Wijmans and R. W. Baker, *J. Membr. Sci.*, 1995, **107**, 1–21.

52 T. C. Merkel, V. I. Bondar, K. Nagai, B. D. Freeman and I. Pinnau, *J. Polym. Sci., Part B: Polym. Phys.*, 2000, **38**, 415–434.

53 J. Moore, C. Stanitski and P. Jurs, *Principles of chemistry: the molecular science*, Cengage Learning, 2009.

54 J. Griswold and J. E. Kasch, *Ind. Eng. Chem.*, 1942, **34**, 804–806.

55 T. K. Poddar and K. K. Sirkar, *J. Chem. Eng. Data*, 1996, **41**, 1329–1332.

56 M. Sokuler, G. K. Auernhammer, C. J. Liu, E. Bonaccurso and H. J. Butt, *EPL*, 2010, **89**, 36004.

57 V. V. Bergeron and D. Langevin, *Phys. Rev. Lett.*, 1996, **76**, 3152–3155.

58 A. Carlson, P. Kim, G. Amberg and H. A. Stone, *EPL*, 2013, **104**, 34008.

59 T. Tadros, P. Izquierdo, J. Esquena and C. Solans, *Adv. Colloid Interface Sci.*, 2004, **108–109**, 303–318.

60 H. M. Princen and S. G. Mason, *J. Colloid Sci.*, 1965, **20**, 353–375.

61 R. Farajzadeh, R. Krastev and P. L. J. Zitha, *Adv. Colloid Interface Sci.*, 2008, **137**, 27–44.

62 J. D. Paulsen, R. Carmigniani, A. Kannan, J. C. Burton and S. R. Nagel, *Nat. Commun.*, 2014, **5**, 3182.

63 G. E. Charles and S. G. Mason, *J. Colloid Sci.*, 1960, **15**, 236–267.

64 O. Reynolds, *Philos. Trans. R. Soc. London*, 1886, **177**, 157–234.

65 J. Eggers, J. R. Lister and H. A. Stone, *J. Fluid Mech.*, 1999, **401**, 293–310.

66 D. Y. C. Chan, E. Klaseboer and R. Manica, *Soft Matter*, 2011, **7**, 2235–2264.

67 J. B. Boreyko, G. Polizos, P. G. Datskos, S. A. Sarles and C. P. Collier, *Proc. Natl. Acad. Sci. U. S. A.*, 2014, **111**, 7588–7593.

68 J. Peng, Y. Han, Y. Yang and B. Li, *Polymer*, 2004, **45**, 447–452.

69 D. L. Weaire and S. Hutzler, *The physics of foams*, Oxford University Press, 1999.